Comprehensive comparisons of GAM characteristics and dynamics between Tore Supra experiments and gyrokinetic simulations

A. Storelli,[1, a)] L. Vermare,[1] P. Hennequin,[1] Ö. D. Gürcan,[1] G. Dif-Pradalier,[2] Y. Sarazin,[2] X. Garbet,[2] T. Görler,[3] Rameswar Singh,[1] P. Morel,[1] V. Grandgirard,[2] P. Ghendrih,[2] and the Tore Supra team[2]

[1)]*Laboratoire de Physique des Plasmas, École Polytechnique, CNRS, UPMC, UPSud, 91128 Palaiseau, France*

[2)]*CEA, IRFM, F-13108 Saint-Paul-Lez-Durance, France*

[3)]*Max Planck Institute for Plasma Physics, Boltzmannstr. 2, 85748 Garching, Germany*

In a dedicated collisionality scan in Tore Supra, the geodesic acoustic mode (GAM) is detected and identified with the Doppler backscattering technique. Observations are compared to the results of a simulation with the gyrokinetic code GYSELA. We found that the GAM frequency in experiments is lower than predicted by simulation and theory. Moreover, the disagreement is higher in the low collisionality scenario. Bursts of non harmonic GAM oscillations have been characterized with filtering techniques, such as the Hilbert-Huang transform. When comparing this dynamical behaviour between experiments and simulation, the probability density function of GAM amplitude and the burst autocorrelation time are found to be remarkably similar. In the simulation, where the radial profile of GAM frequency is continuous, we observed a phenomenon of radial phase mixing of the GAM oscillations, which could influence the burst autocorrelation time.

[a)]Electronic mail: alexandre.storelli@lpp.polytechnique.fr

I. INTRODUCTION

One of the main challenges facing the development of modern tokamaks and their lack of sufficiently good confinement for achieving self-sustained thermonuclear fusion is the understanding and the control of anomalous transport, generally thought to be driven by small scale turbulent phenomena and its mesoscale nonlinear dynamics. Zonal flows (ZF), for example, are axisymmetric mesoscale flow structures ($m = n = 0$), that are known to be generated by turbulence and that in turn quench the turbulence which generate them[1,2]. Such a relation implies a dynamical coupling, mimicking the population dynamics between a predator (i.e. ZF) and a prey (i.e. turbulence) species, which may be playing a role in the Low to High confinement (L-H) transition[3] observed in tokamaks and stellerators[4,5]. Two families of these flows are identified: a stationary branch (which may nonetheless be involved in some predator-prey evolution), called the low-frequency ZF, and a branch which oscillates at a frequency of the order c_s/R, where c_s is the sound speed and R is the major radius. This latter branch is called the geodesic acoustic mode[6] (GAM), which is the subject of the comparisons in this article. GAM, by itself, does not reduce turbulence intensity as much as low-frequency ZF[7], but it is believed to exchange energy with the low-frequency ZF and the drift-wave turbulence thus acting as a third player in a possible predator-prey dynamics[8,9]. As a result of this, it could be a key ingredient in the L-H transition. Therefore knowing precise properties of GAM and comparing them with simulations may help in understanding the different parts of the puzzle, which may in turn help predicting, and potentially increasing, the performance of future machines.

Substantial progress has been made on understanding GAMs during the last decade. They have been detected in a variety of machines, as reviewed for example in Ref.[10]. Its properties have been compared to theory and gyrokinetic simulations: for example, the GAM-turbulence interaction and GAM propagation simulated with GTC was consistent with HL-2A experiments[11,12]. ELMFIRE calculations could reproduce the GAM frequency and radial structure found in FT-2[13,14]. Here, we study GAM frequency, intensity and dynamics in the core of Tore Supra plasmas and quantitatively compare the observations between experiments and simulations. Notice that these results differ from the earlier ones in that they are the first to achieve such detail in a reasonably large tokamak with substantial heating.

GAM has been previously detected in the high collisionality case of a dedicated $\nu^\star$ scan in Tore Supra[15,16], using the Doppler backscattering technique. As part of our study, a simulation has been run with the gyrokinetic code GYSELA[17], based on parameters corresponding to the experiments.

The rest of the paper is organized as follows. Section II describes how GAM is detected in experiments and simulation, including a description of the experimental setup, simulation and numerical tools used to analyse GAM oscillations. In section III, GAM is identified in experiments and its

frequency is compared with that found in simulation and predicted by theory. In section IV, we compare the RMS value and the probability distribution function of GAM intensity. In section V, we present the burst autocorrelation time of GAM oscillations in experiments and simulation, as well as the properties of GAM radial propagation observed in simulation.

II. DETECTION OF GAM IN EXPERIMENTS AND IN SIMULATION

A. Doppler backscattering experimental setup

Results presented in the following have been obtained during a dimensionless collisionality scan performed in the tokamak Tore Supra for studying the scaling of transport and turbulence[15]. In those experiments, the profile of $\nu^\star = \frac{\nu_{ii} q R}{\varepsilon^{3/2} V_{t,i}}$ has been varied by a factor of 4, while $\rho^\star = \rho_i / a$ and $\beta = p/\left(B^2/2\mu_0\right)$ profiles were kept constant. At $\rho = 0.8$, $\nu^\star$ varied from 0.2 (low $\nu^\star$ case) to 1 (high $\nu^\star$ case), while $\rho^\star = 2 \cdot 10^{-3}$ and $\beta = 5 \cdot 10^{-4}$. The plasmas studied here are L-mode, limited discharges with ion cyclotron resonance heating (ICRH). Flux surfaces are circular with $R_0 = 2.39\ m$ and $a = 0.72\ m$ (figure 3c). The safety factor profile is kept constant during shots, with an edge safety factor $q_a = 4$. The high $\nu^\star$ case has a weaker ohmic current, weaker magnetic field, a stronger ICRH heating and higher temperatures than its lower $\nu^\star$ counterpart. Temperature and $\nu^\star$ profiles are given in figure 1. More details of these dedicated experiments can be found in Ref. Vermare *et al.* [15].

In experiments, GAMs are studied using signals from two Doppler Backscattering Systems (DBS). This technique allows us to measure the velocity of turbulent fluctuations at a given wavenumber in a direction perpendicular to both the radius and the magnetic axis[18]. The Doppler shift in spectra, ω_{DBS}, is related to the perpendicular velocity of density fluctuations with the relationship $\omega_{DBS} = k_\perp V_\perp$, where $k_\perp$ is the wave-number of the probed fluctuation, which is usually computed with a beam tracing code[19]. The measured velocity, $V_\perp$, is the sum of the mean $E \times B$ velocity of the plasma (dominated at the edge by ripple ion transport mechanisms in Tore Supra[20]), plus a finite phase velocity of fluctuations whose sign may change with the nature of the turbulent regime: $V_\perp = V_{E\times B} + V_\phi$.

The first DBS, described in Ref. Vermare *et al.* [16], has two channels operating respectively in the V and W bands. The first channel (V-band) features an O-mode beam that probes the core of the plasma. The second channel (W-band) features an X-mode beam that probes the edge of the plasma, towards the scrape-off layer (SOL). The second DBS has one channel, similar to the first one (V-band in O-mode) and is located at the top of the machine with a vertical line of sight, in a different toroidal sector ($\triangle\varphi = 210°$).

Studying the GAM oscillation requires the ability to obtain the temporal sequence of the perpen-

dicular velocity $V_\perp(t)$ with a sufficient time resolution. To extract the frequency associated with the Doppler shift $\omega_{DBS}(t)$ from the DBS signal with a high temporal resolution; a time-frequency analysis can be done, either using the fast Fourier transform (FFT) on reduced time sliding window (SWFFT), or using dedicated time-frequency techniques, such as the MUltiple SIgnal Classification (MUSIC) algorithm[16]. For the analysis presented in this paper, we have used the latter with the following settings: 50 % overlapping windows of 128 points, an autocorrelation matrix of size $n_w = 8$ and a number of frequencies to detect $n_f = 1$ (in some cases, $n_f = 2$). The resulting sampling rate of $V_\perp(t)$ is 156 kHz in acquisitions that last between 3.3 and 53 ms.

B. Parameters of the GYSELA simulation

A dedicated simulation has been run with the semi Lagrangian, global full-f flux-driven 5D gyrokinetic code GYSELA[17,21] to compare GAM properties with experimental results in detail. The simulation is global with a radial extension $0.15 \leq \rho \leq 1$, and flux-driven so as to preclude scale-separation assumptions and allow for the temperature profile to freely evolve, with a dynamics due to the volumic heat source, while it is fixed at the outer edge where contact with a thermal bath provides heat sink. The heat source, applied through a modification of the distribution function[21], is tailored to reproduce the radial profile of additional experimental heating. The amplitude of the heat source can be adapted to match the experimental temperature profile. Electrons are adiabatic (with $T_e \equiv T_i$), so that simulated turbulence is mainly ITG-like. In the present study, GYSELA will be used only to simulate a case at high $\nu^\star$ and low β, in which ITG is dominant and trapped electron negligible (as shown in sec. IV), and to compare GAM characteristics between simulation and experiments. Note that passing kinetic electrons may have some effects even for ITG turbulence through ETG turbulence, which will not be reproduced in this simulation. However, passing electrons and ETG are not expected to have a significant impact on GAMs, so the adiabatic assumption appears reasonable for the purpose of this work. The collision operator preserves mass, momentum and energy and only accounts for ion-ion collisions[22]. Boundary conditions for the parallel velocity are no-slip on both radial limits, with Dirichlet $\phi = 0$ boundary conditions on the potential. In the core, a typical staircase pattern of interacting flows and avalanches is observed, correlated to temperature corrugations[23,24].

The simulation is performed with parameters as close as possible to the experimental high $\nu^\star$ case described before. In particular there was an effort to match the radial profiles of normalized temperature, normalized density, safety factor and collisionality to those of the experiment (cf. figure 1).

In practice, the shape of the radial profiles of density, safety factor and collisionality are directly taken from experiments. Concerning the shape of the temperature profile, the amount of heat source

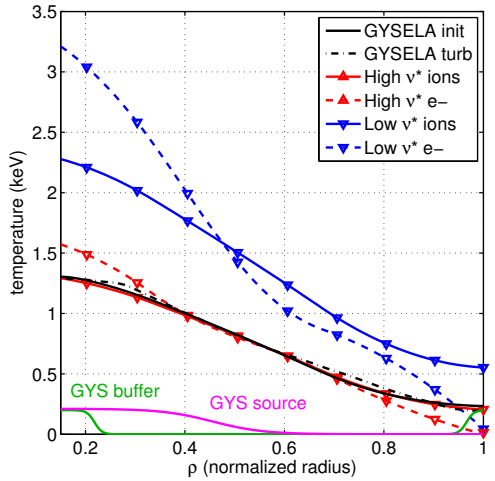

(a) Temperature

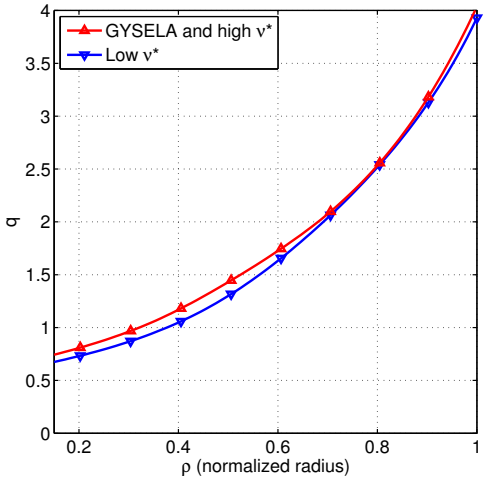

(b) Safety factor q

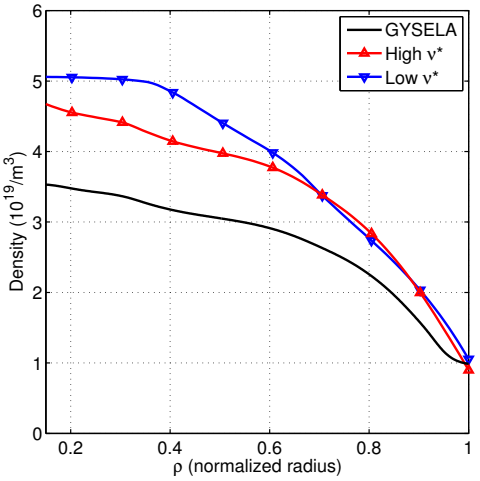

(c) Density

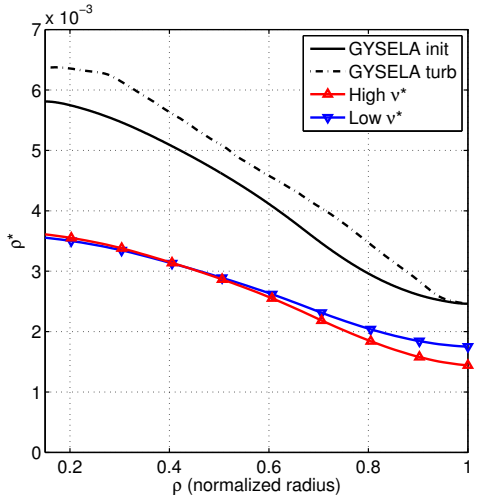

(d) $\rho^\star$ profiles

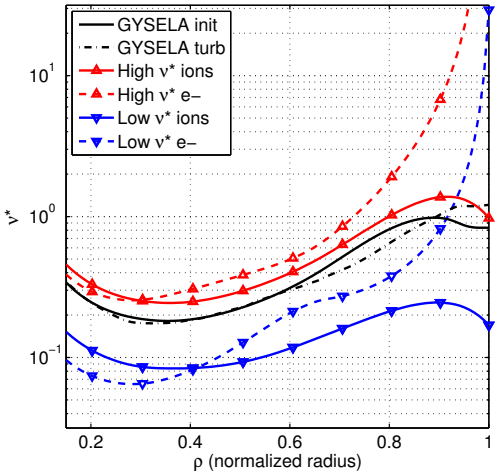

(e) $\nu^\star$ profiles

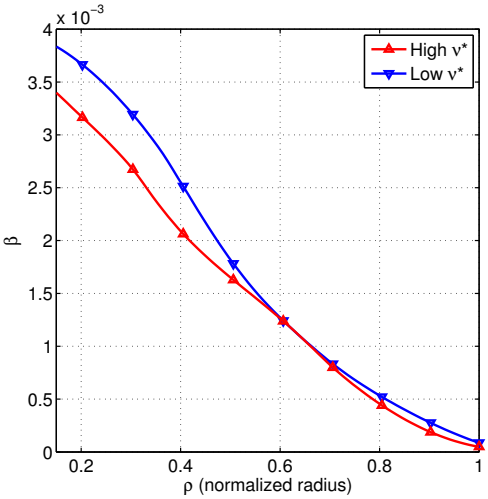

(f) β profiles

Figure 1. Main plasma parameters compared in simulation and in experiments (high and low $\nu^\star$ cases). When relevant, two regimes of the simulation have been separated: that of early oscillations before the turbulence onset (solid black lines) and that of established turbulence, when the initial oscillations of GAM have vanished (dashed black lines).

is adapted to match the shape of the experimental one. When analyzing the outputs of the GYSELA simulation, particular attention was required to put the simulation data in a dimensional form similar to that of the experiment, in order to correctly mimic the absolute plasma parameters of the Tore Supra high $\nu^\star$ shots. First, the temperature profiles have been denormalized with the values of experiments. Secondly, aspect ratio $R_0/a = 3.3$ and major radius $R_0 = 2.3945\ m$ have been taken equal to those of the experiment. The magnetic field is constrained by the value of $\rho^\star$ (chosen as an input of the simulation) and by the denormalized values of the temperature and of the minor radius. Finally, the radial profile of the normalized collisionality $\nu^\star$, which has been directly computed using the density and temperature profiles from the experiments, is used to denormalize the density profile. It should be noted that the simulation has been performed for Hydrogen (without impurities) while the experimental plasma was mostly composed of Deuterium. This discrepancy lead to a factor $\sqrt{2}$ in the absolute value of collisionality and therefore in the absolute value of density.

To summarize, the parameters which differ from their experimental counterparts are the on-axis magnetic field $B_0 = 1.2\ T$ (without any impact since the code is electrostatic), the absolute values of collisionality and density (lower by a factor $\sqrt{2}$ in GYSELA), and the value of $\rho^\star = 1/300$ (almost twice as much as the experimental values). $\rho^\star$ is used to determine the radial grid size: its increase in GYSELA reduces the numerical cost of the computation.

The $\sqrt{2}$ difference in the absolute value of $\nu^\star$ is expected to have a finite but small effect on GAM, for example in the GAM damping. On the other hand, the same difference in the absolute value of the density profile should not have any consequence since the normalized density gradient is equal to the experimental one. In addition to these discrepancies, it should also be mentioned that the amount of heat injected through the volumic heat source to recover the experimental temperature profile, $0.8\ MW$, differs slightly from the experimental one: $2\ MW$.

This large-scale simulation was run on the Helios supercomputer (the 5D space is sampled by $\sim 8.6 \times 10^{10}$ points, with a 512-point radial axis leading to $\delta\rho \approx 0.002$). As a flux-driven system, GYSELA has to be run on an energy confinement time in order to guarantee full convergence of the fluctuation profiles. In the computation reported here, this profile has not yet saturated past $0.7 \leq \rho$ so that the excitation of the GAM is not realistic in that region. Therefore, the comparison of GAMs between experiments and simulation is restricted to properties which are not expected to vary much with the strength of the source: frequency and, more cautiously, dynamics.

To study GAM in GYSELA, the phase velocity of turbulent fluctuations is neglected and $V_\perp$ is simply taken equal to the $E \times B$ velocity, so that $V_\perp = -\partial_r \langle\phi\rangle / B$, where $\langle\phi\rangle$ is the surface-averaged electrostatic potential, sampled roughly at $450\ kHz$.

C. Numerical processing of $V_\perp$ signals

Given $V_\perp(t)$ from experiments and simulation, we first study the mean frequency of the GAM oscillation from classical spectral analysis with an average spectral estimator: Welch's power spectral density estimate. An illustrative example of the power spectrum of an experimental signal is drawn in figure 2a with a solid black line. In that case, the peak at 12 kHz is considered as that of GAM.

Then, to study the dynamical behaviour of the GAM oscillation and its intermittency, we proceed with a time-frequency analysis on $V_\perp(t)$. However, the relatively low sampling rate of the $V_\perp(t)$ time sequence and its limited length make it difficult to apply: the sliding FFT method (SWFFT) lacks temporal resolution and MUSIC lacks stability on short segments. Instead, we gain access to the *instantaneou*s frequency of the GAM and its amplitude with the same sampling rate as the original signal by directly applying the Hilbert transform on $V_\perp(t)$ and calculating the phase derivative of the resulting analytical (complex) signal. A more sophisticated version of this method is used here to filter out the noise and keep the dominant oscillatory signal: $V_\perp$ is preprocessed with an algorithm called *empirical mode decomposition* (EMD). EMD decomposes the signal in a sum of functions that, individually, behave well with the Hilbert transform. Therefore EMD gave $V_\perp(t) = \sum_n I_n(t)$ with each I_n being an *intrinsic mode function* (IMF), representing the signal in a spectral interval (see illustration in figure 2a). The whole process is named *Hilbert-Huang transform* (HHT)[25–27].

In section V, to better emphasize the dynamics of GAM, $V_\perp(t)$ is bandpass-filtered around the GAM frequency. Two methods are used, so two signals are available: $V_{\perp,GAM}^{FFT}(t)$, given by a classical bandpass filter with zero phase delay (based on FFT), and $V_{\perp,GAM}^{HHT}(t)$, found by adding the IMFs I_n with weights that depend on their instanteneous frequency ω_n:

$$V_{\perp,GAM}^{HHT}(t) = \sum_n \left[G(\omega_n(t))\, I_n(t)\right] \tag{1}$$

where G, illustrated in figure 2b, is the frequency response of the filter used for $V_{\perp,GAM}^{FFT}(t)$. ω_n is calculated with the derivative of the unwrapped phase of each I_n, in finite differences at the fourth order, with a moving average selected for maximum stability[25]. In order to compute the probability distribution functions in section IV, we used the instantaneous envelope of the filtered $V_\perp$. Such envelope is evaluated by

$$V_{\perp,GAM}^{\pm}(t) = \pm \sum_n \left[G(\omega_n(t))\, a_n(t)\right] \tag{2}$$

where a_n is the instantaneous amplitude of IMF I_n. The application on a sample signal is drawn in figure 2b). The IMFs I_n in eq. 1 are not exactly in phase, so the sum of their amplitudes a_n in eq. 2 (dashed red) is slightly wider than the sum of the I_n (solid red). To display spectral contents of

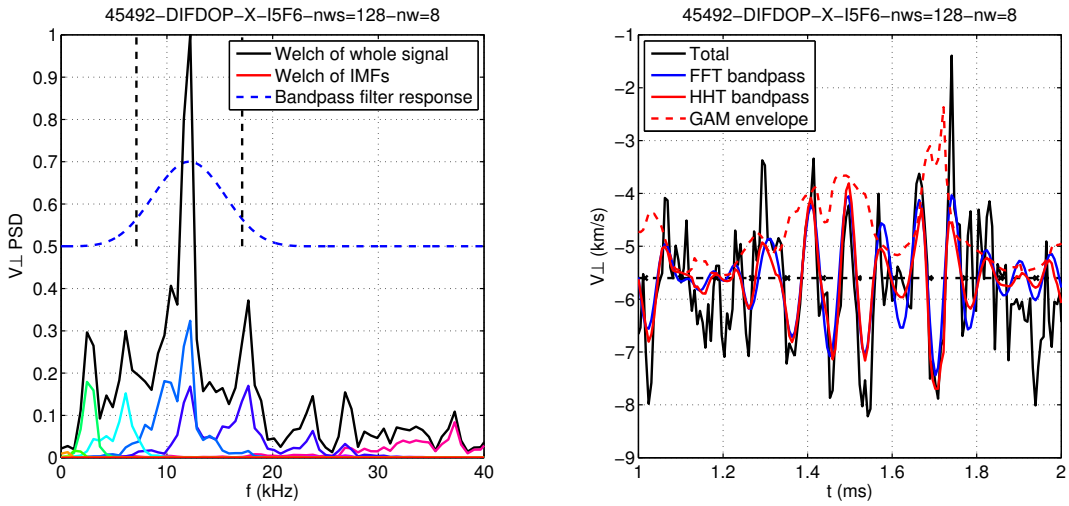

(a) Spectra of individual IMFs (in color) and of the whole signal (solid black)

(b) Signal bandpass and instantaneous envelope

Figure 2. Example of HHT processing applied to an experimental signal in low $\nu^\star$ scenario at $\rho = 0.95$.

GYSELA simulation in section III (figure 4c-d), we computed HHT pseudo-spectra with

$$P(\omega) = \omega^2 \int_0^T \left[\sum_{j=1}^{n} \delta\left(\omega, \omega_j(t)\right) a_j^2(t) \right] dt \tag{3}$$

where the Kronecker symbol $\delta(i, j)$ is 1 when $i = j$ and 0 otherwise.

III. GAM FREQUENCY PROFILES

A. Identification of GAM in experiments

As GAM and Beta Alfvén Eigenmode (BAE) share the same dispersion relation[28,29], identifying GAM by its frequency is, to be strict, not enough. Here, we show the $m = 1$ structure of δn and the $n = m = 0$ structure of $V_\perp$ in the experimental high $\nu^\star$ case. We used measurements on the same flux surface in the equatorial plane and at the top of the plasma (see poloidal projection in figure 3c – the toroidal angle between the two diagnostics is 210°).

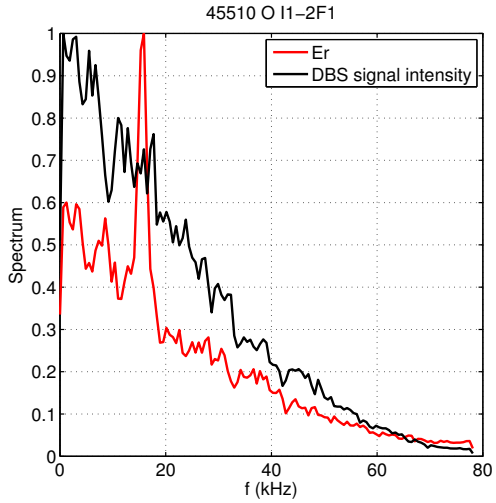

(a) LFS, O-mode at $\rho \sim 0.82$

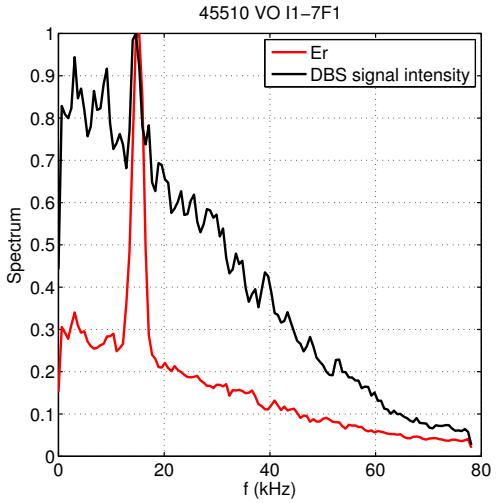

(b) TOP, O-mode at $\rho \sim 0.82$

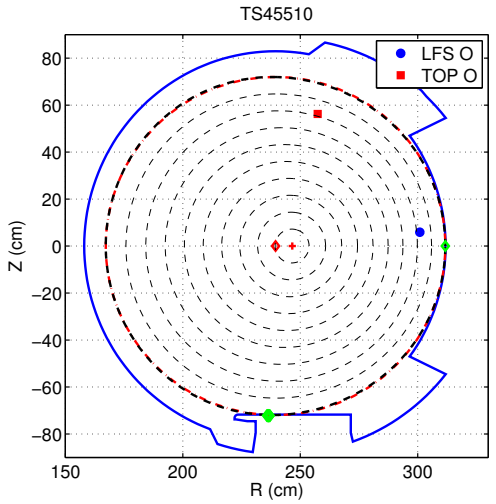

(c) Poloidal view of DBS measurements

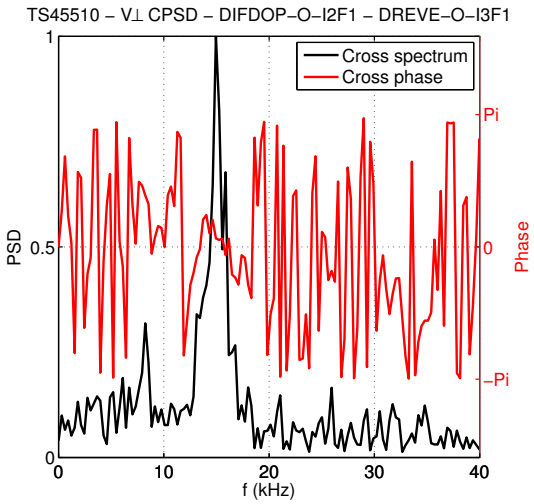

(d) LFS-TOP $V_\perp$ cross spectrum

Figure 3. Identification of GAM in experiments. (a-b) Superposition of spectral density (normalized) of $V_\perp$ and of DBS signal intensity, in shot 45510 (high $\nu^\star$), in the equatorial plane (a) and from the top of the machine (b). (c) Poloidal projection of localization of measurements. Green diamonds stand for contact points. (d) Cross spectrum and cross phase between $V_\perp$ signals between the equatorial plane and the top of the machine.

GAM density perturbations δn have been estimated by the eigenvalue obtained by MUSIC associated with fluctuations content. δn was not modulated at GAM frequency in the equatorial plane (figure 3a, compatible with previous results[16]), while a spectral peak of δn at GAM frequency was visible in measurements from the top of the plasma (figure 3b). This strongly suggests a $m = 1$ structure for GAM density fluctuations.

For the $V_\perp$ structure, we computed the cross-spectrum and the cross-phase between equatorial and top measurements. The cross spectrum shows a clear peak at 15 kHz (figure 3d in black). The cross phase is close to zero at the frequency of the peak, while it spans the $[-\pi,\ \pi]$ interval at other frequencies. This observation is an indication of the $n = m = 0$ structure of $V_\perp$ at the GAM frequency. To conclude, the top-bottom $m = 1$ structure for density fluctuations and the $n = m = 0$ structure for the flows evidence the presence of GAM in high $\nu^\star$ experiments.

B. Comparison of GAM frequency profiles

Observations in experiments

In experiments, GAMs are observed in the edge of both low and high $\nu^\star$ plasmas (as reported earlier for the high $\nu^\star$ case[16]). To determine the experimental spectra, we compiled all exploitable measurements for each collisionality scenario, shot by shot. Spectra are averaged over these identical shots. In figures 4a (low $\nu^\star$) and 4b (high $\nu^\star$), GAM is visible in the range of 10-15 kHz, with an increasing frequency towards the core, where temperature is higher. To determine the GAM frequency profile, we have taken the maximum of X-mode spectra (blue pluses in figures). The frequency profiles roughly match the empirical scaling found in literature[30–33], drawn in solid green lines in figures 4a-b :

$$f_{exp} = \sqrt{\frac{T_i + T_e}{m_i}} \frac{1}{2\pi R}. \tag{4}$$

However, exact theoretical predictions give higher frequencies. Literature gives several GAM frequency predictions in fluid models (ideal MHD[6] and Braginskii two-fluid framework[34]) and in kinetic ones[35–38]. All known predictions are close in experimental conditions. Therefore, for clarity, only the MHD prediction of Winsor[6] and the kinetic one of Sugama[37] have been drawn in figures 4a-d. Winsor prediction is:

$$f_{W1968} = \sqrt{2 + \frac{1}{q^2}} \sqrt{\frac{(5/3)\,(T_i + T_e)}{m_i}} \frac{1}{2\pi R} \tag{5}$$

and that of Sugama, considered in the fluid limit $\left(qR\,(2\pi f)\,/\sqrt{2T_i/m_i}\right)^2 \gg 1$ with less than 0.5 % error, is:

$$f_{S2006} = \sqrt{2 + \frac{(23/4)\,T_i^2 + 4T_iT_e + T_e^2}{q^2\left[(7/4)\,T_i + T_e\right]^2}}\sqrt{\frac{(7/4)\,T_i + T_e}{m_i}}\frac{1}{2\pi R} \underset{q^2 \gg 1}{\approx} \sqrt{2}\sqrt{\frac{(7/4)\,T_i + T_e}{m_i}}\frac{1}{2\pi R}. \quad (6)$$

Considering this model, GAM has a lower frequency than predicted by kinetic theory, by 20 to 40 % in high $\nu^\star$ and by 40 to 50 % in low $\nu^\star$. It is noted that the disagreement seems to decrease when $\nu^\star$ increases.

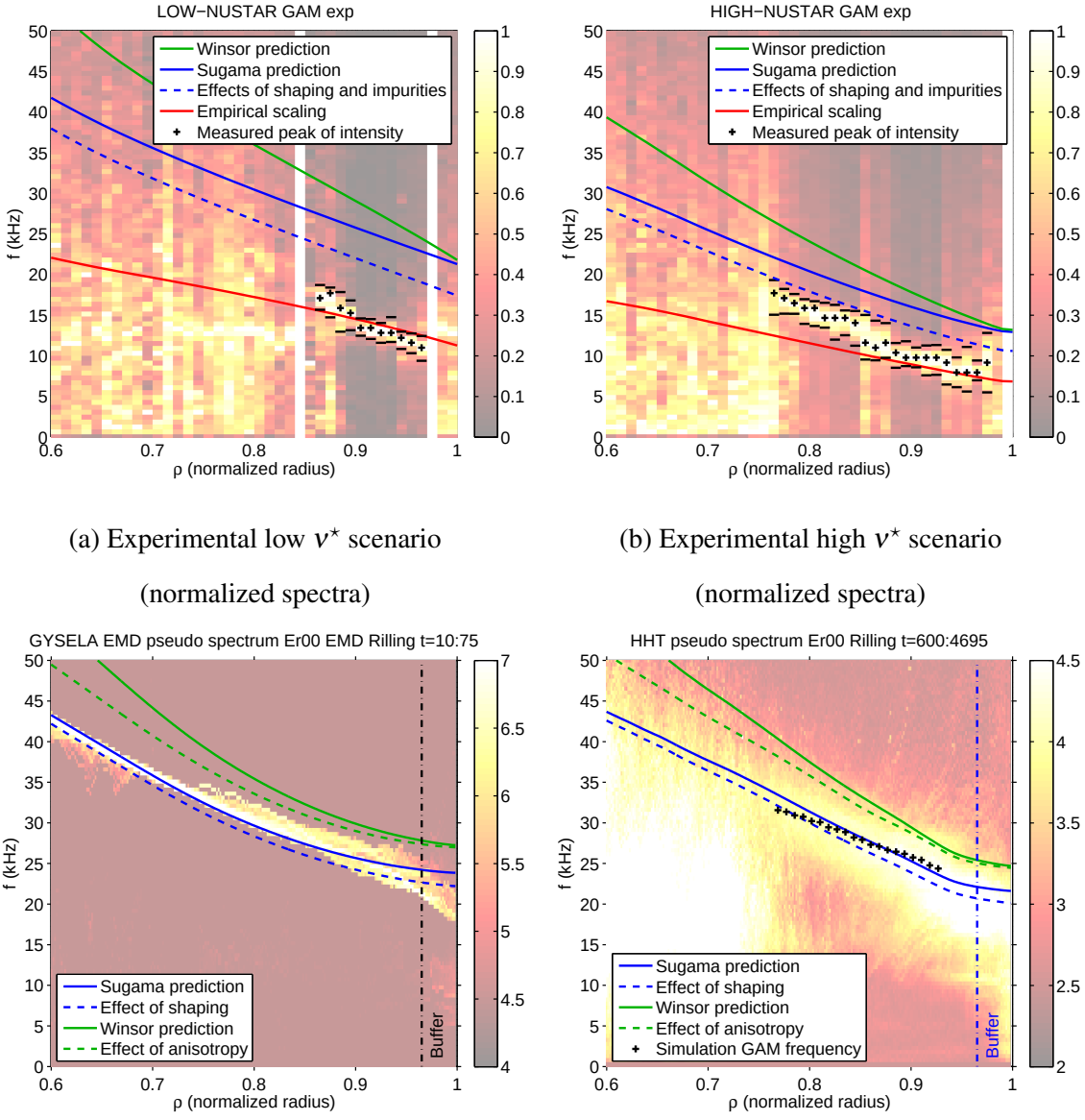

(a) Experimental low $\nu^\star$ scenario (normalized spectra)

(b) Experimental high $\nu^\star$ scenario (normalized spectra)

(c) High $\nu^\star$ simulation in early oscillations

(d) High $\nu^\star$ simulation in established turbulence

Figure 4. Comparison of GAM frequency measured in experiments (a-b, shot by shot averaged spectral densities) and observed in simulation (c-d, HHT pseudo-spectra as defined in eq. 3).

In addition, some frequency steps are observed in the experimental profiles of GAM frequency. In the low $\nu^\star$ case, a step is visible near $\rho = 0.91$ with $f \sim 14\ kHz$. In the high $\nu^\star$ case, two steps

are visible at $\rho = 0.82$ with $f \sim 15\ kHz$ and at $\rho = 0.91$ with $f \sim 10\ kHz$. The width of the steps is $\Delta\rho \approx 0.05$ in the high $\nu^\star$ case. In low $\nu^\star$, it is between $\Delta\rho = 0.03$ and 0.05 (an uncertainty appears as measurements are missing at some precise radii). Those values are higher than the radial resolution of X-mode DBS ($\delta\rho \sim 0.015$) and match with the typical mesoscale dimension $\Delta\rho = \sqrt{\rho_\star}$. Moreover, they are consistent with the experimental findings on ASDEX[39] and with a numerical study of Landau fluid electrostatic ITG turbulence[40]. In the low $\nu^\star$ case, spectral content at $f \sim 14\ kHz$ was not only visible near the frequency step. It appeared as well for $0.72 < \rho < 0.82$ and for $0.98 < \rho < 1$, but with a small signal to noise ratio. Given the available dataset, it is not possible to conclude on the precise nature of this observation.

Observations in simulation

In the dedicated GYSELA run, GAM is observed through the surface-averaged E_r, noted $\langle E_r \rangle$, in early linear oscillations with $20 < t < 152\ \mu s$ (66 time steps, figure 4c) and in established turbulence $1.34 < t < 10.49\ ms$ (4096 time steps, figure 4d). In both regimes, GAM is always much stronger on $\langle E_r(\theta) sin\theta \rangle$ than on $\langle E_r(\theta) \cos\theta \rangle$, confirming its $m = 1$ top-bottom poloidal structure ($\theta = 0$ at the LFS and 90° at the top). Electrons being adiabatic in GYSELA, T_e has been taken equal to T_i in the calculation of GAM frequency predictions. Winsor's prediction, with $\Gamma_e = 5/3$, is roughly 10 % higher than other predictions with $\Gamma_e = 1$, including that of Sugama (eq. 6). Therefore, in the case of simulation, Winsor and Sugama predictions have been drawn for each regime analysed. In both regimes, GAM frequency is very close to Sugama prediction (solid blue line). However, GAM frequency is lower than the prediction in the buffer region, where an artificial Krook operator is applied to damp the fluctuations. Observations should be considerered unreliable in that region, indicated by the green line in figure 1a and by dashed black lines at $\rho = 0.965$ in figures 4c-d.

The early time steps of the simulation behave like a Rosenbluth-Hinton relaxation[22,41] without turbulent activity. Intense GAM oscillations are present in a wide radial range ($0.25 < \rho < 1$) and absent in the inner buffer region. GAM amplitude decreases with time. Later, in established turbulence regime, GAM is still present but it is visible only on the outer part of the radial box, for $\rho > 0.75$. The boundary coincides with the upper radial expansion of broadband signature of turbulence, that may hide the GAM for $\rho < 0.75$, if it exists. The representative GAM frequency in simulation is determined by the first moment $f = \int_{f-}^{f+} Pf / \int_{f-}^{f+} P$ of $\langle E_r \rangle$ Fourier spectra with $f-$ and $f+$ being user-defined boundaries on each side of the GAM spectral peak. This frequency profile is plotted with a dashed blue line in figure 4d. We discarded the results for $\rho > 0.93$ because of the presence of the buffer.

Discussion

In all experimental cases, we noted that GAM is observed at a lower frequency than predicted by a standard kinetic prediction of the GAM frequency. In simulation, GAM frequency follows the same kinetic prediction with a reasonable agreement. From here, we investigate effects that may help the predictions reconcile with experimental observations.

First, the effect of plasma geometry, evaluated with the prediction of Gao[42], is applicable in both experiments and simulation. The finite aspect ratio and Shafranov shift lead to a reduction of Sugama prediction by a factor $1-\frac{3\varepsilon^2}{4}-\frac{\Delta'^2}{8}+\frac{5\varepsilon\Delta'}{8}\lesssim 1$, where $\varepsilon=r/R$ is the inverse aspect ratio (up to 0.3) and $\Delta'=-2\rho\Delta_0/a$ is the radial gradient of the Shafranov shift ($\Delta_0/a=0$ in simulation and typically $\Delta_0/a=0.1$ in experiments). Applying such calculation for experiments leads to a practical reduction of GAM frequency between 5.5 % at $\rho=0.7$ and 10 % at $\rho=0.95$. This brings predictions closer to experimental observations. In simulation, the downshift of GAM frequency is 5.5 % at $\rho=0.9$. It does not significantly change the quality of the agreement between simulation and prediction.

Impurities have also a role on the GAM frequency[43] which is only applicable to experiments, as this GYSELA simulation did not include them. For example, in the FT2/ELMFIRE comparison, impurities were an essential ingredient to match GAM frequencies[13,14,44]. On Tore Supra plasmas, the main impurities are carbon and oxygen elements (due to carbon limiters and active cooling of the walls with water). In Tore Supra, line averaged $Z_{eff}=\left(\sum_i n_i Z_i^2\right)/\left(\sum_i n_i Z_i\right)$ is measured from visible spectroscopy. Its value was found to be around 2 (± 0.5). From the definition of Z_{eff}, in a two species plasma, we have : $\alpha_{imp}=n_{imp}/n_{bulk}=\left(Z_{eff}-1\right)/\left[Z_{imp}\left(Z_{imp}-Z_{eff}\right)\right]$, where n_{imp} and Z_{imp} are the density and charge number of impurities, respectively. If $q^2\gg 1$ (valid at the edge), if GAM is weakly damped and if impurities and bulk ions have the same temperature T_i, Guo's formulas give $f_{GAM,i}=\sqrt{2}\sqrt{\frac{(7/4)T_i}{m_1}+\frac{T_e}{m_2}}\frac{1}{2\pi R}$ with the effective masses of ions $m_1=\frac{m_{bulk}+\alpha_{imp}m_{imp}}{1+\alpha_{imp}}>m_{bulk}$ and $m_2=\frac{m_{bulk}+\alpha_{imp}m_{imp}}{1+\alpha_{imp}Z_{imp}}=m_{bulk}$ (indeed we have in this study $m_{imp}/m_{bulk}=Z_{imp}$). Hence, the original GAM frequency prediction is decreased by the presence of impurities. Thus, accounting for impurities helps predictions, match with experimental observations. If $T_i=T_e$ and $Z_{eff}=2$, the reduction of GAM frequency with carbon-only impurities ($Z_{imp}=6$), is 5.5 %, while with oxygen ($Z_{imp}=8$) the reduction is 4 %. The dependence of $f_{GAM,i}$ on Z_{eff} is significant: with $Z_{eff}=1.5$ and 2.5 in carbon-only scenario, corrections are 2.7 % and 8.3 % respectively. The downshift of the frequency prediction caused by impurities should not exceed 10 %. The dashed blue line in figure 4 shows the total correction of the GAM frequency prediction by the effects of shaping and impurities, in experiments only, with carbon particles, $Z_{eff}=2$ and finite T_e/T_i and q. The combined effect of geometry and impurities is not enough to explain the discrepancy between predictions and measurements. For example, with carbon impurities, a Z_{eff} of 4 would be required to make the high $\nu^\star$ profiles match,

while Z_{eff} would need to converge towards 6 in the low $\nu^\star$ case. Both values are unrealistic, especially for the low $\nu^\star$ case.

The twofold effect of pressure anisotropy has to be discussed. First, the anisotropy of GAM pressure perturbations modifies the adiabatic coefficient Γ_i in the formulas that predict GAM frequency. Writing $f_{GAM} \approx \sqrt{2}\sqrt{\left(\Gamma_i T_i + \Gamma_e T_e\right)/m_i}/2\pi R$, isotropic models have $\Gamma_i = 5/3$, such as in single fluid MHD[6] and two-fluid MHD[34]. In frameworks that allow anisotropic pressure perturbations, Γ_i is equal to $7/4$, such as in MHD[45], two-fluid MHD[46] and in kinetic models, including that of Sugama and Watanabe[37]. As $7/4 > 5/3$, anisotropic models give slightly higher predictions than equivalent isotropic ones. The other effect of pressure anisotropy deals with background pressure, as shown in MHD[45], and is visible when the ratio $\chi = p_\perp/p_\parallel$ departs from 1. More precisely, in Ren's model, defining $\mathscr{G}_1 = \frac{3\chi}{2} + 2 + \frac{3}{q^2}$ and $\mathscr{G}_0 = \frac{\sqrt{3}}{6q^2}\left(1 + \chi - \frac{\chi^2}{3}\right)$, the GAM frequency reads:

$$f_{R2014} = \sqrt{\left(\frac{\mathscr{G}_1 + \sqrt{\mathscr{G}_1^2 - 4\mathscr{G}_0}}{2}\right)\frac{T_{i\parallel} + T_{e\parallel}}{m_i}}\frac{1}{2\pi R} \underset{q^2 \gg 1}{\approx} \sqrt{2}\sqrt{\frac{\left(\frac{7+3(\chi-1)}{4}\right)\left(T_{i\parallel} + T_{e\parallel}\right)}{m_i}}\frac{1}{2\pi R}. \quad (7)$$

This model appears as an evolution from that of Winsor, where, assuming $q^2 \gg 1$, $\Gamma = 5/3$ and T are simply replaced by $\Gamma = \left(7 + 3\left(\chi - 1\right)\right)/4$ and $T_\parallel$. χ has been computed in simulation. In the radial interval of interest ($0.75 < \rho < 0.93$), $\chi = 1$ in the early oscillations and $\chi \approx 0.85$ in the turbulent regime, leading to a slight modification of the frequency prediction according to eq. 7. The total effect of pressure anisotropy is in the downshift direction, rather small near the edge and more visible towards the core. The profiles of Winsor and Ren predictions are drawn in solid and dashed green lines on figure 4c-d. In experiments, χ is not accessible. ICRH should cause $\chi > 1$ for the minority ion in the area of power deposition[47], but it is near the magnetic axis while GAM is observed closer to the edge ($0.78 < \rho$). Moreover, heat is transferred to electrons and bulk ions through collisional processes that may damp anisotropies, leading to $\chi \approx 1$. Therefore, at the current level of understanding, the effects of background pressure anisotropy are not expected to play a lead role in the present experimental observations.

The effect of GAM radial wave number on the GAM frequency should also be considered. Literature did not provide a definitive and clear picture of this effect. We first considered the theories of Sugama[37] and Zonca[48] and resolved the equations with Davies[49] and multivariable Newton-Raphson numerical methods. Significant effects arise for $k_r\rho_i > 0.1$. In Sugama's work, k_r has a slightly decreasing effect of GAM frequency and its main effect is to strongly enhance collisionless damping. In Zonca's work, k_r increases GAM frequency while collisionless damping remains reasonably small ($< 1\ kHz$). We noted in a more recent model[50] that k_r has a non-monotonous effect on GAM frequency, coupled with finite β and $\nu^\star$ effects. Therefore, the effect of k_r on GAM frequency is difficult to estimate. In addition, the evaluation of k_r is not achievable in the experiments with the given

experimental setup (radial correlation measurements would be required). In simulation, the propagative behaviour of GAM in turbulent regime described in section V B suggests that $0 < k_r\rho_i < 0.1$. A compatible ordering, k_r of the order 1 cm^{-1}, has been observed in other machines such as JFT-2M[51], HL-2A[11,12,52–54], T-10[32], DIII-D[55] and TCV[56]. In conclusion, the effect of GAM radial wave number should be small.

Collisionality may play a role in simulation. In strongly collisional regimes ($\nu_{ii} \gg V_{Ti}/R$), Gao[57] predicted that the GAM frequency decreases down to the empirical scaling (eq. 4). Generally, the opposite scaling applies ($\nu_{ii} \ll V_{Ti}/R$) so this effect is negligible here. However, the buffer region in simulation, characterized by a stabilizing Krook operator, may be an exception. In the case this effect would be significant in the buffer region, it would explain why simulated GAM is observed at a lower frequency than predicted.

Other contributions of toroidal[58] and poloidal[59] rotation, expected to increase GAM frequency, are neglected. Indeed, Tore Supra has no significant external momentum input and the toroidal and poloidal rotations remain largely subsonic[60].

In summary, the experimental high $\nu^\star$ case could almost be recovered with geometry and impurities effects, especially in the core for $\rho < 0.9$ (see dashed blue curve in figure 4). Including the respective corrections, a reasonable fit is found in the high $\nu^\star$ case between experiments, simulation and theory. However, the low $\nu^\star$ remains problematic, as the reviewed corrections are not enough to explain the gap between observations and predictions. One may look for effects specific to low collisionalities. For example, low $\nu^\star$ is characterized by trapped particles statistically following wide portions of banana orbits. Watari et al.[61], studying the effect of finite orbits and trapped particles, noted the existence of two GAM bands, one of which may be comparable to experimental GAM scaling. In the framework of Alfvén modes, Chavdarovski et Zonca[62] found that a combined effect of deeply trapped ions and inertia of the plasma could cause a $O(\varepsilon)$ effect on mode frequency. Because of the GAM/BAE degeneracy[29], this effect might apply to GAM as well. Such effects should be visible in GYSELA as it takes into account trapped ions orbits. Unfortunately, the simulated high $\nu^\star$ case presented herein is where those effects may be negligible. In future work, simulations at various $\nu^\star$ could exhibit this effect.

IV. GAM INTENSITY PROFILES

In experiments, we estimated the intensity of GAM by the RMS (root mean square) value of bandpass-filtered $V_\perp$ signals (with FFT method, cf. section II C): $A_{GAM} = RMS\left(V^{FFT}_{\perp,GAM}(t)\right)$. Results are reported on figure 5a. The main observation is that GAM is more intense in the low $\nu^\star$ case than in the high $\nu^\star$ one. In high collisionality experiments, GAM amplitude grows progressively from 150 m/s at $\rho = 0.75$ to 450 m/s at $\rho = 0.95$, with slight corrugations. The low $\nu^\star$ profile features a peak at $\rho \sim 0.92$ and $\Delta V \sim 800$ m/s, where amplitude is twice as much as in the high $\nu^\star$ case. On each side of this intensity peak, GAM intensity in low $\nu^\star$ is closer to high $\nu^\star$ results.

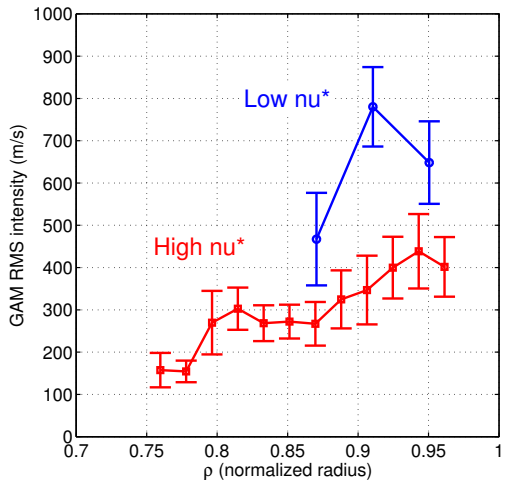

(a) Comparison of GAM amplitude

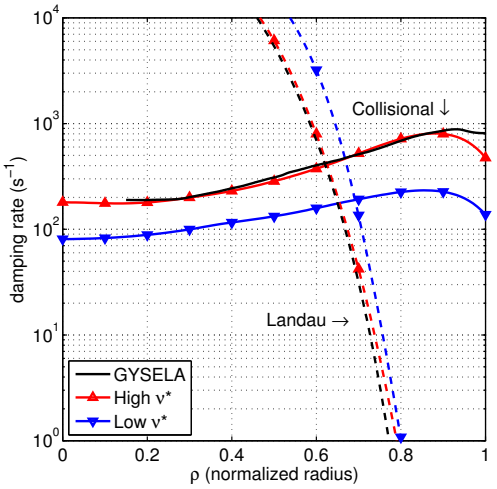

(b) Theoretical GAM damping terms

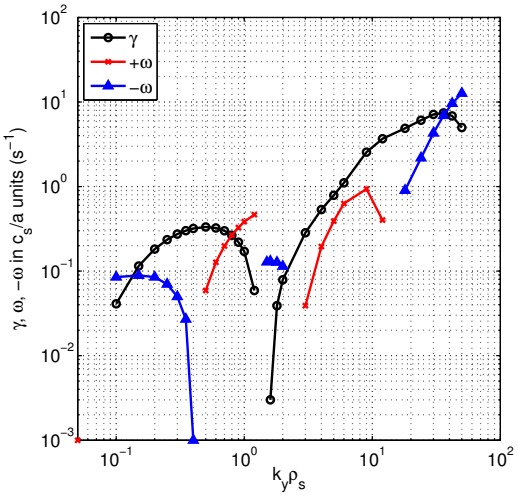

(c) Low $\nu^\star$ linear growth rate (GENE)

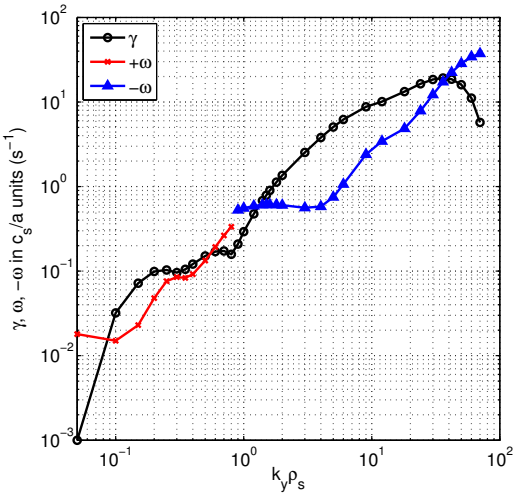

(d) High $\nu^\star$ linear growth rate (GENE)

Figure 5. GAM intensity: (a) experimental observations, (b) estimated damping and (c-d) linear growth rate γ and frequency of turbulence ω calculated with GENE at $\rho = 0.8$, where positive (negative) ω indicate propagation in the ion (electron) diamagnetic drift direction and where, in this context, $c_s = \sqrt{T_e/m_i}$.

The interpretation of the GAM intensity requires information about both source and damping of GAM. Here, the source is related to turbulent intensity[8]. The experimental profiles of $\delta n/n$ are not

precise enough to be used for low/high $\nu^\star$ comparisons, because of significant uncertainties related to the contribution of the low k scales. Therefore, the source has been estimated using local simulations performed with the gyrokinetic code GENE[63], considering fully kinetic deuterium ions and electrons for both scenarii at $\rho = 0.8$. The results in figure 5c-d show that the high $\nu^\star$ case is clearly ITG dominant, while the low $\nu^\star$ case features a complex turbulent regime at low k scales, which seems to be a hybrid ITG/TEM. In this range, the linear growth rate is higher in the low $\nu^\star$ case by a typical factor of two. The GAM excitation is then expected to be stronger in the low $\nu^\star$ case.

Concerning the damping, fig. 5b shows that, in the edge, it is dominated by collisional effects[57,64], while Landau damping[65] is negligible as $q^5 \exp\left(-q^2\right) \ll 1$. Collisional damping is stronger in the high $\nu^\star$ case than in the low $\nu^\star$ case. Therefore, the intensity of GAMs appears as a clear picture: GAM is more intense in low $\nu^\star$ case where turbulent source is stronger and damping weaker.

In simulation, GAM has an intensity a few tens m/s, which is much weaker than in experiments by an order of magnitude. Such disagreement could be explained by the smaller level of fluctuations δn in the range of the simulation we analysed. To check the validity of this hypothesis, we considered a simple energy equilibrium of GAM, excited by Reynolds stress S and linearly damped with a rate γ:

$$\partial A/\partial t + \gamma A = S. \tag{8}$$

The quantity $A_{GAM}\gamma/S$ represents the steady state intensity of GAM, normalized to S/γ, the ratio between source and damping. We compared this normalized intensity between experiments and simulation. For simplicity, S is considered proportional to δn^2. At $\rho = 0.85$, $\delta n/n$ is typically 2% in experiments while $\delta n/n$ is 0.6% in the range of simulation considered (note that $n_{GYS}/n_{EXP} \sim 0.8$). Values for γ are in fig. 5b. In this model, the ratio $\left(S_{EXP}/\gamma_{EXP}\right)/\left(S_{GYS}/\gamma_{GYS}\right)$ is of order 17. This ratio matches qualitatively with the observed ratio of intensities $A^{EXP}_{GAM}/A^{GYS}_{GAM} \approx 14$. Therefore, even if GAM is much weaker in simulation than in experiments, its intensity seems to scale consistently with the local fluctuations level.

Going further than the RMS value of GAM intensity, we computed the probability density function (PDF) of $\Delta V_\perp(t)$, the time series of GAM intensity. In other words, we studied the statistics of temporal variation of GAM intensity around its mean value drawn in fig. 5. Such a PDF provides information about the nonlinear interaction between background turbulence and the GAM. For example, in the case of a harmonic predator-prey interaction[66], one would expect to observe the PDF of a sinusoid (*bull* shaped). We have defined $\Delta V_\perp(t)$ as the instantaneous envelope of GAM oscillations provided by HHT filtering (equation 2). We computed the corresponding PDF $P\left(\Delta V_\perp(t)\right)$ on data from experiments and simulation. The results are displayed in figure 6 (note that $\Delta V_\perp$ axis is in logarithmic scale for readability purposes). Data shows that, in all situations, the PDF can be approximated by $P(\Delta V_\perp) \approx \alpha \Delta V_\perp^2 \exp\left(-\Delta V_\perp^2/\Delta V_{\perp,0}^2\right)$ with α ensuring that the integral of P is 1 and

$\Delta V_{\perp,0}$ is an average GAM amplitude close to that presented in figure 5a. Therefore, the PDF of GAM intensity in simulation and experiments depend on a remarkably single parameter, a most probable GAM intensity $\Delta V_{\perp,0}$. Note that in all cases the PDF could also be well represented by Γ distributions, $P(\Delta V_\perp) \propto \Delta V_\perp^k \exp(-\Delta V_\perp / V_0)$ with k between 3.5 and 5.5 and $V_0 \approx \Delta V_{\perp,0}/k$, also represented in figure 6. As the PDF observed are away from that of a sinusoid, this result shows the absence of clear and harmonic predator-prey oscillations. In particular, this observation is compatible with the fact that Tore Supra L-mode plasmas are not close to L-H transition.

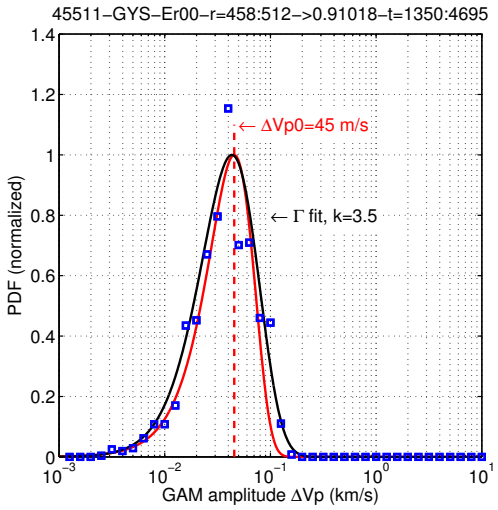

(a) High $\nu^\star$ simulation (in established turbulence)

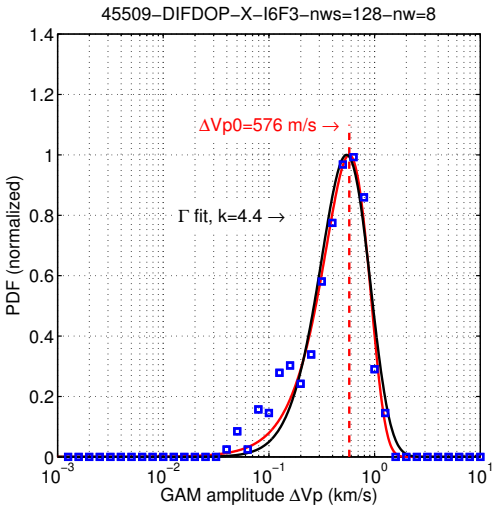

(b) Experimental high $\nu^\star$ case

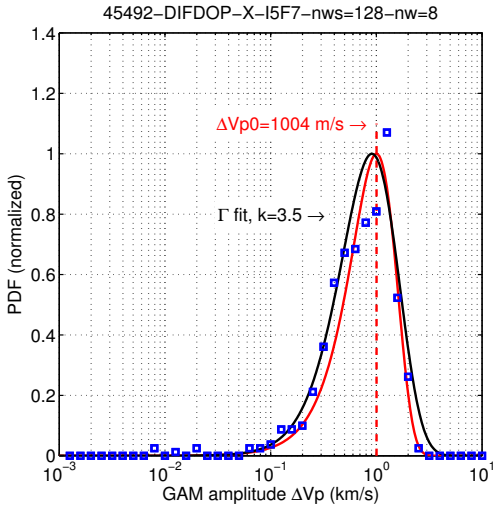

(c) Experimental low $\nu^\star$ case (at peak of intensity)

Figure 6. Probability density function of GAM amplitude at $\rho \approx 0.91$. Amplitude axis is in log scale. Blue squares represent the PDF of GAM amplitude, red curves are the fit with $\Delta V_\perp^2 \exp\left(-\Delta V_\perp^2 / \Delta V_{\perp,0}^2\right)$ and black curves the fit with $\Delta V_\perp^k \exp(-\Delta V_\perp / V_0)$.

V. DYNAMICS

A. GAM bursty behaviour

The intermittent behaviour of GAM has been known for long (for example Conway *et al.*[31], McKee *et al.*[67]), but comparably few authors have characterized it[11,32,55,68]. In this section, GAM burst autocorrelation time is computed from the bandpass filtered $V_\perp$ (equation 1) and compared between experiments and simulation.

We have used three methods to compute the autocorrelation profile of $V_\perp$. The figure 7 shows an example of the direct autocorrelation of $V_\perp$ (black line), of the autocorrelation of FFT bandpass-filtered $V_\perp$ (solid blue line) and of the autocorrelation of HHT bandpass-filtered $V_\perp$ (solid red line). The direct autocorrelation method features a very fast decorrelation time, smaller than a GAM period, and does not seem meaningful. We rather focused on the results of the autocorrelation of filtered signals. Different time scales seem to exist: in the experimental and simulation data we analysed, a fast decay of autocorrelation profile is generally noted within 0.3 *ms*, while a small but finite correlation variations sustain for 1 *ms* and more. The fast decay time is small compared to the length of acquisitions, so its statistics are more reliable compared to the long-lasting correlation time which approaches the length of many data segments. Therefore, we only deal with the fast decay time, which we call the *burst autocorrelation time* τ. Depending on the numerical method, it is noted τ_{FFT} or τ_{HHT}. The envelope is fitted with $f(\Delta t) = Ae^{-\Delta t/\tau} + (1-A)$ for $0 < \Delta t < 1$ *ms* and $0 \leq A \leq 1$. Results are displayed on figure 7 in blue and red dashed lines for FFT- and HHT-filtered signals, respectively. τ_{FFT} and τ_{HHT} are close to a GAM period, which is consistent with visible GAM oscillations in figure 2a. We noted that $\tau_{HHT} < \tau_{FFT}$. Indeed, HHT filter preserves the non-linearities in the oscillation and FFT-filter sometimes exaggerates oscillations. Both determinations are displayed in figure 8 where results are compared between simulation and experiments.

A reasonable agreement is found for burst autocorrelation time between simulation and both collisionality cases. Across all exploited data, τ always has the 0.1 *ms* order of magnitude, as visible on figure 8. Autocorrelation times found here are comparable to those found in JIPP-TIIU[68] and in HL-2A[69], but smaller than those in DIII-D[55] and in other HL-2A plasmas[11], and much smaller than those found in T-10[32].

For experimental results of figure 8, we displayed the average of τ among groups of ~ 20 data segments for each radial point, weighted by the acquisition length. Error bars correspond to the variance between determinations of τ for each group of data segments. Radial profiles show interesting corrugations. It appears that the low $\nu^\star$ profile has a peak at $\rho \sim 0.92$ with $\tau_{FFT} = 0.24 \pm 0.10$ *ms* being twice as much the values at adjacent radii $\tau_{FFT} \approx 0.13 \pm 0.05$ *ms*. High $\nu^\star$ profile has smaller

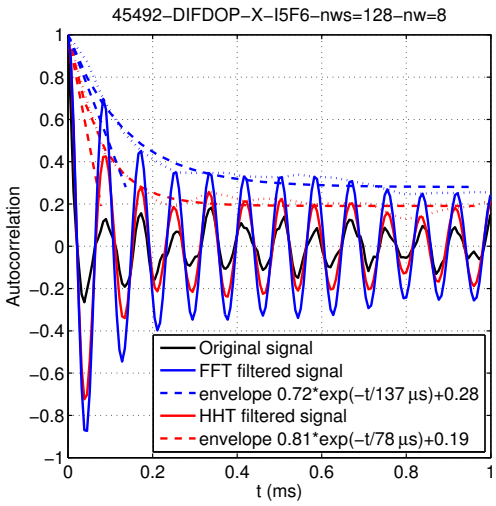

Figure 7. Illustration of $V_\perp$ autocorrelation in experimental low $\nu^\star$ case at $\rho = 0.95$. In the data presented, a GAM period lasts 84 μs.

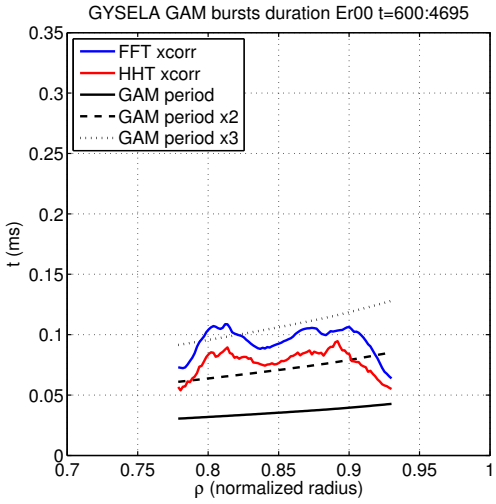

(a) High $\nu^\star$ simulation

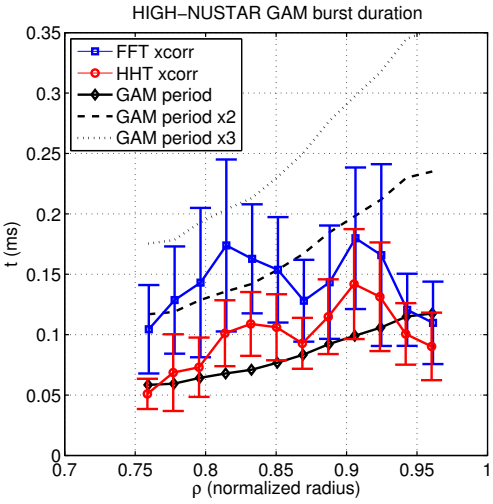

(b) Experimental high $\nu^\star$ scenario

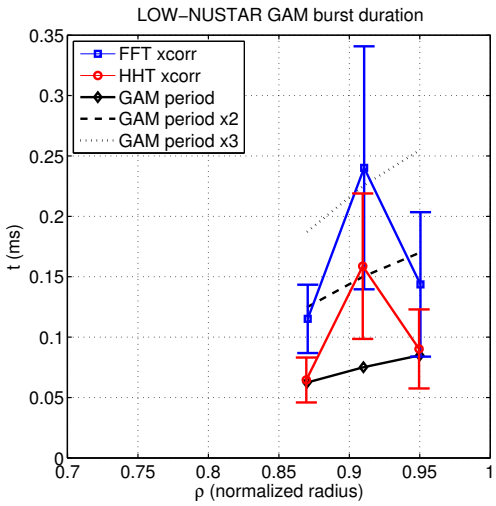

(c) Experimental low $\nu^\star$ scenario

Figure 8. Autocorrelation time compared between simulation and experiments.

corrugations, with peaks at $\rho \sim 0.82$ and $\rho \sim 0.91$ and a bottom at $\rho \sim 0.87$ with a 1.5 factor. The peaks of τ profiles match with the locations at which GAM frequency profile is flatter than the continuum GAM profile (figure 4). In the case of low $\nu^\star$ where this observation is the clearest, it matches the radius of GAM maximum intensity (figure 5). This could be an experimental evidence of a radial zone where the GAM excitation is stronger than elsewhere. τ is smaller in simulation than in high $\nu^\star$ experiments with a typical 1.5 factor. However, when normalized to the GAM period, GAM is more coherent in simulation ($1.5 < \tau f_{GAM} < 3.2$) than in high $\nu^\star$ experiments ($0.8 < \tau f_{GAM} < 2.5$). In low $\nu^\star$ experiments, the averaged τf_{GAM} tops at 3.2. The magnitude of τ could be illustrated the following way, by rewriting the equation 8 in a Langevin form, related to the Brownian motion, so that $(\partial/\partial t + \gamma)A = S(t)$. One may consider that the correlation time of $S(t)$ is that of turbulent fluctuations, a few microseconds[70], and that the damping time γ^{-1} is close to a millisecond (fig. 5). The autocorrelation time, at hundred microseconds, lies between those two orders of magnitude. The physics that define τ might not be the same between simulation and experiments. In simulation, GAM autocorrelation time may be linked to the radial propagation time (see section V B) while the mechanism is not identified in experiments.

B. GAM propagation in simulation

In simulation, the knowledge of GAM oscillations in the time and radius axis allows us to study the radial propagation of GAM. We analysed this propagation under two points of view: phase propagation, showing how the phase of the mode organizes itself given a radial gradient of GAM frequency, and group propagation, related to the energy of the mode. In both cases, GAM features an outwards propagative behaviour.

The radial organization of the phase of the GAM is represented in figure 9a. The respective maxima and minima of $E_{r10}(\rho,t) = \langle E_r \sin\theta \rangle$, bandpass filtered around GAM frequency, are radially connected and displayed as red and blue lines. Four temporal filtered E_{r10} signals have been superimposed for the sake of clarity. On average, red and blue lines are rather straight, which means that oscillations are radially correlated. However, the direction of the lines varies with time. For example, at $t = 7$ *ms*, there is no significant phase delay between radii, while at $t = 7.1$ *ms*, oscillations are slightly out of phase. This phenomenon is obviously caused by the radial gradient of GAM frequency, which progressively desynchronizes GAM oscillators between radii. GAM frequency is lower at $\rho = 0.93$ than at $\rho = 0.85$, so the direction of the red and blue lines turns clockwise with time in figure 9b. This phenomenon has a limit where a critical slope is reached. For example, at $t = 7.15$ *ms* and $\rho = 0.86$, a phase jump happens. Such jumps happen regularly, at various radii, and coincide with a low intensity of GAM, as shown by the superimposed grey curves. The system

seems to admit a maximum phase delay Δt across Δr so that $\min(\Delta r/\Delta t) \approx 1.3\ km \cdot s^{-1}$. On average, $\Delta r/\Delta t \approx 2.9\ km \cdot s^{-1}$. This critical shearing rate could be related to the phenomenon of phase mixing damping, also known as continuum damping. Such a mechanism has been described long ago in the field of Alfvén waves, but much more recently on GAM itself[71,72] and may explain the pulsing noted in NLET simulations[73]. This propagative behaviour qualitatively fits with the FT-2/ELMFIRE comparison[14] where an agreement of radial phase velocity is found at roughly $1\ km \cdot s^{-1}$. In experiments, similar outwards propagations have been obtained on TEXTOR[74] and DIII-D[55], but inward propagation is observed on TCV[56]. In simulation, other authors have found GAM phase propagating in both directions with GTC[12] and NLET[75] codes.

The group propagation is studied at the top of figure 9b. The displayed quantity, representative of the intensity of GAM, is the logarithm of $\sum_{j=1}^{n} G\left(\omega_j(t)\right)\left(a_j(t)\,\omega_j(t)\right)^2$, using the notations of section II C, where a_j and ω_j are the result of the HHT of $\partial_r E_r$. A series of propagative events is clearly observed in the first milliseconds of the simulation, separated by $\Delta t \sim 0.6\ ms$ within the black box, bounding the zones $0.85 < \rho < 0.93$ and $1.5 < t < 4.3\ ms$. In this area, we have calculated the intercorrelation of this signal between a reference radius, $\rho_0 = 0.89$, and other radii. A finite propagation of GAM intensity appears at $V_r \approx +0.4\ km \cdot s^{-1}$, which is smaller than the diamagnetic velocity $V^\star = \left|\frac{T_e}{enB}\frac{\partial n}{\partial r}\right| \sim 1.5\ km/s$ applicable for this simulation. It is unlikely that this propagative behaviour is connected with transport through ballistic fronts[76], as seen at deeper radii ($\rho \leq 0.8$) in the same simulation[24]. The group propagation seems rather related to the phenomenon of phase synchronization described above: at the bottom of figure 9, we displayed the instantaneous frequency of GAM, normalized to the prediction of Sugama (eq. 6) and defined by

$$f^\star_{GAM}(t) = \frac{1}{2\pi f_{S2006}} \left[\sum_j \omega_j(t)\, I_j(t)\, G\left(\omega_j(t)\right)\right] / \left[\sum_j I_j(t)\, G\left(\omega_j(t)\right)\right].$$

The phase jumps are identified by red-blue vertical discontinuities in this figure, where $f^\star_{GAM}$ varies locally by a factor of 2 in the radial direction. We observed that the group propagation only happens inside *corridors*, where no phase jump is present and where $f^\star_{GAM} \sim 1$. Such corridors are noted in the black box of figure 9b (top) and in the data used in figure 9a. The amount of group propagation events decreases with time, as the radial gradient of temperature and GAM frequency increase slightly, causing more phase jumps (where GAM is weak) and less room for group propagation.

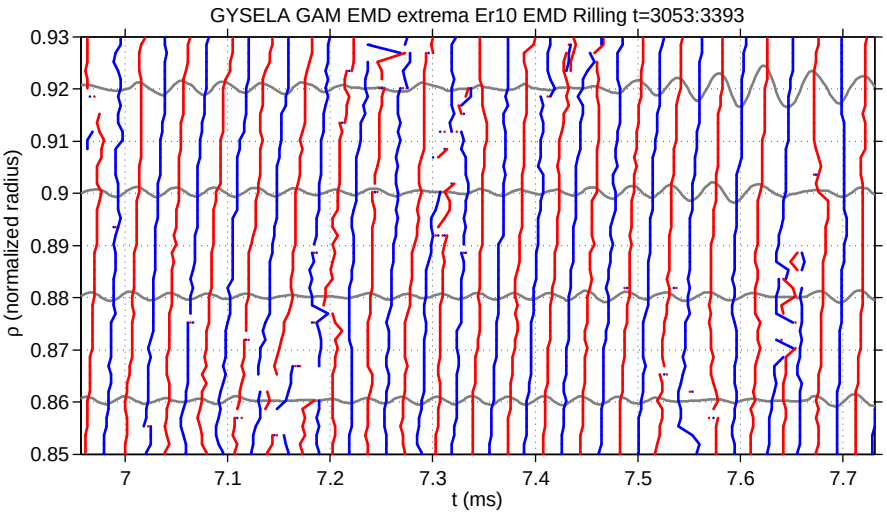

(a) Illustration of the radial synchronization of the phase of GAM oscillation.

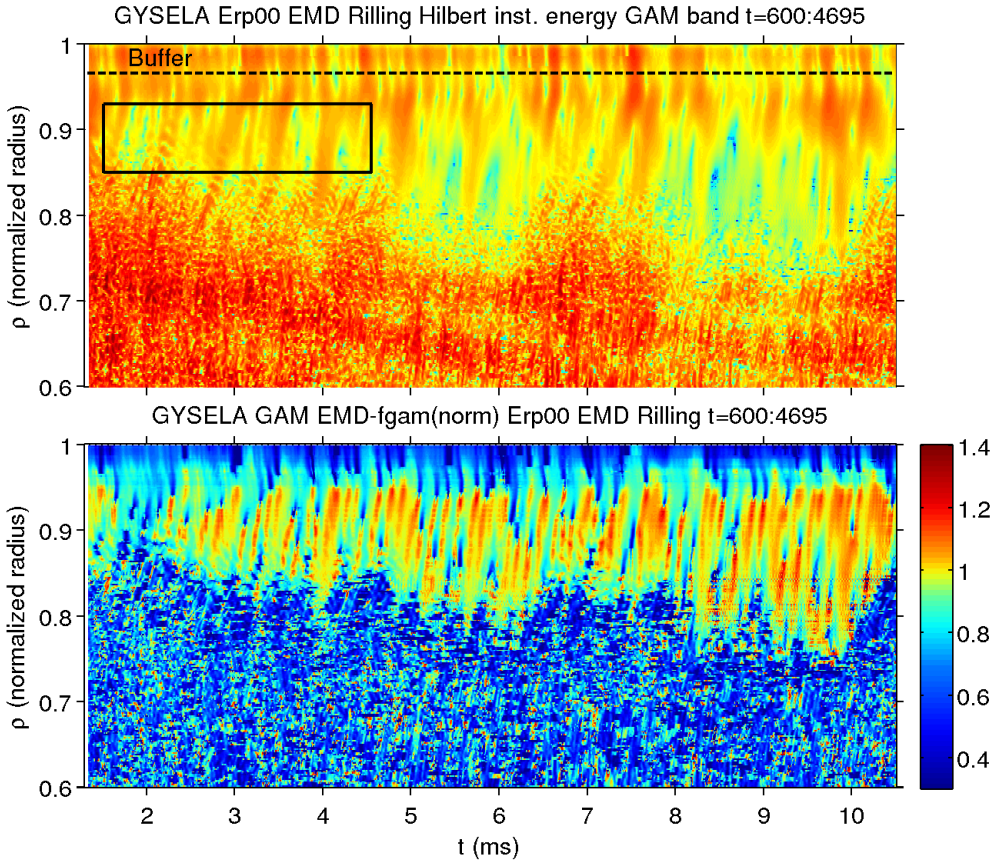

(b) Top: time-radius map of the intensity of GAM (red color stands for high intensities). An intercorrelation of the data inside the black box determined an outwards group propagation of GAM intensity at roughly 400 m/s. Bottom: instantaneous frequency of GAM oscillations, normalized to Sugama prediction (eq. 6).

Figure 9. GAM propagative behaviour in GYSELA high $\nu^\star$ simulation.

VI. SUMMARY AND CONCLUSION

GAM properties have been compared between Tore Supra experiments and a simulation with GYSELA, which is tailored to represent the plasmas of a high collisionality case in a dedicated scan. For GAM frequency, a fair agreement between simulation and theoretical predictions has been found. In experiments, the measured GAM frequency is below predictions. Taking into account the effects of plasma shaping and impurities helps approaching an agreement for the experimental high $\nu^\star$ case. However, such effects are not large enough in the low $\nu^\star$ case counterpart, where the remaining difference is not well understood.

GAM is found to be more intense in the low $\nu^\star$ case than in the high $\nu^\star$ one, which is consistent with the estimated source and damping of the mode. GAM in simulation is weaker than in experiments, obviously because the turbulence intensity is undervalued in the time interval we analysed. A simple evaluation of the source and damping ratio of the mode, in both experiments and simulation shows that intensity of the mode scales consistently with the local fluctuations level. In experiments and simulation, the PDF of GAM intensity is almost in $\Delta V_\perp^2 \exp\left(-\Delta V_\perp^2/\Delta V_{\perp,0}^2\right)$ or in $\Delta V_\perp^k \exp\left(-k\Delta V_\perp/\Delta V_{\perp,0}\right)$, with $k \sim 4$, which means that no clear predator-prey oscillation is present between GAM and fluctuations.

GAM oscillations appear in amplitude bursts in both experiments and simulation, with a similar burst autocorrelation time of the order $0.1\ ms$. In experiments, GAM seems more coherent at some precise radii where it is more intense and where frequency steps are noted. In contrast, no frequency steps are observed in the simulation, where the radial continuum of GAM frequency profile leads to a pattern of mode intermittency, characterized by an outwards phase synchronization at several km/s and some outwards propagative events at $0.4\ km/s$. As the phase mixing instationarity is mostly restricted to simulation, it is not clear if the mechanisms defining the burst autocorrelation time in the experiments and the simulation are the same.

In conclusion, this quantitative comparison between experiments, theoretical models and simulation highlighted some limits of the current predictions of GAM frequency. Some potential missing ingredients such as the effect of finite orbit and trapped particles and/or the effect of the radial wavenumber of the GAM are discussed, but deeper investigation is required to elucidate this overestimated prediction. In addition, the interest for the experimental technique of radial correlation with Doppler backscattering appears, which could lead to further measurements of GAM propagation.

ACKNOWLEDGMENTS

We thank D. Zarzoso, P. H. Diamond, R. Dumont and C. Bourdelle for fruitful discussions. This work has been carried out within the framework of the EUROfusion Consortium and has received funding from the European Union's Horizon 2020 research and innovation programme under grant agreement number 633053. The views and opinions expressed herein do not necessarily reflect those of the European Commission.

REFERENCES

[1]P. H. Diamond, S.-I. Itoh, K. Itoh, and T. S. Hahm, Plasma Physics and Controlled Fusion **47**, R35 (2005).

[2]K. Itoh, S.-I. Itoh, P. H. Diamond, T. S. Hahm, A. Fujisawa, G. R. Tynan, M. Yagi, and Y. Nagashima, Physics of Plasmas **13**, 055502 (2006).

[3]E.-j. Kim and P. H. Diamond, Phys. Rev. Lett. **90**, 185006 (2003).

[4]G. D. Conway, C. Angioni, F. Ryter, P. Sauter, and J. Vicente (ASDEX Upgrade Team), Phys. Rev. Lett. **106**, 065001 (2011).

[5]T. Estrada, C. Hidalgo, T. Happel, and P. H. Diamond, Phys. Rev. Lett. **107**, 245004 (2011).

[6]N. Winsor, J. L. Johnson, and J. M. Dawson, Physics of Fluids **11**, 2448 (1968).

[7]T. S. Hahm, M. A. Beer, Z. Lin, G. W. Hammett, W. W. Lee, and W. M. Tang, Physics of Plasmas **6**, 922 (1999).

[8]K. Itoh, K. Hallatschek, and S.-I. Itoh, Plasma Physics and Controlled Fusion **47**, 451 (2005).

[9]R. E. Waltz and C. Holland, Physics of Plasmas **15**, 122503 (2008).

[10]A. Fujisawa, Nuclear Fusion **49**, 42 (2009).

[11]A. D. Liu, T. Lan, C. X. Yu, H. L. Zhao, L. W. Yan, W. Y. Hong, J. Q. Dong, K. J. Zhao, J. Qian, J. Cheng, X. R. Duan, and Y. Liu, Phys. Rev. Lett. **103**, 095002 (2009).

[12]F. Liu, Z. Lin, J. Q. Dong, and K. J. Zhao, Physics of Plasmas **17**, 112318 (2010).

[13]S. Leerink, V. V. Bulanin, A. D. Gurchenko, E. Z. Gusakov, J. A. Heikkinen, S. J. Janhunen, S. I. Lashkul, A. B. Altukhov, L. A. Esipov, M. Y. Kantor, T. P. Kiviniemi, T. Korpilo, D. V. Kuprienko, and A. V. Petrov, Phys. Rev. Lett. **109**, 165001 (2012).

[14]E. Z. Gusakov, A. B. Altukhov, V. V. Bulanin, A. D. Gurchenko, J. A. Heikkinen, S. J. Janhunen, S. Leerink, L. A. Esipov, M. Y. Kantor, T. P. Kiviniemi, T. Korpilo, D. V. Kouprienko, S. I. Lashkul, A. V. Petrov, and N. V. Teplova, Plasma Physics and Controlled Fusion **55**, 124034 (2013).

[15]L. Vermare, P. Hennequin, O. D. Gürcan, C. Bourdelle, F. Clairet, X. Garbet, R. Sabot, and the Tore Supra Team, Physics of Plasmas **18**, 012306 (2011).

[16]L. Vermare, P. Hennequin, O. D. Gürcan, and the Tore Supra Team, Nuclear Fusion **52**, 063008

(2012).

[17]V. Grandgirard, Y. Sarazin, P. Angelino, A. Bottino, N. Crouseilles, G. Darmet, G. Dif-Pradalier, X. Garbet, P. Ghendrih, S. Jolliet, G. Latu, E. Sonnendrücker, and L. Villard, Plasma Physics and Controlled Fusion **49**, B173 (2007).

[18]P. Hennequin, C. Honoré, A. Truc, A. Quéméneur, N. Lemoine, J.-M. Chareau, and R. Sabot, Review of Scientific Instruments **75**, 3881 (2004).

[19]C. Honoré, P. Hennequin, A. Truc, and A. Quéméneur, Nuclear Fusion **46**, S809 (2006).

[20]E. Trier, L.-G. Eriksson, P. Hennequin, C. Fenzi, C. Bourdelle, G. Falchetto, X. Garbet, T. Aniel, F. Clairet, and R. Sabot, Nuclear Fusion **48**, 092001 (2008).

[21]Y. Sarazin, V. Grandgirard, J. Abiteboul, S. Allfrey, X. Garbet, P. Ghendrih, G. Latu, A. Strugarek, and G. Dif-Pradalier, Nuclear Fusion **50**, 054004 (2010).

[22]G. Dif-Pradalier, P. H. Diamond, V. Grandgirard, Y. Sarazin, J. Abiteboul, X. Garbet, P. Ghendrih, G. Latu, A. Strugarek, S. Ku, and C. S. Chang, Physics of Plasmas **18**, 062309 (2011).

[23]G. Dif-Pradalier, P. H. Diamond, V. Grandgirard, Y. Sarazin, J. Abiteboul, X. Garbet, P. Ghendrih, A. Strugarek, S. Ku, and C. S. Chang, Phys. Rev. E **82**, 025401 (2010).

[24]P. Ghendrih, C. Norscini, T. Cartier-Michaud, G. Dif-Pradalier, J. Abiteboul, Y. Dong, X. Garbet, O. D. Gürcan, P. Hennequin, V. Grandgirard, G. Latu, P. Morel, Y. Sarazin, A. Storelli, and L. Vermare, The European Physical Journal D **68**, 303 (2014).

[25]N. E. Huang, Z. Shen, S. R. Long, M. C. Wu, H. H. Shih, Q. Zheng, N.-C. Yen, C. C. Tung, and H. H. Liu, Proceedings of the Royal Society of London. Series A: Mathematical, Physical and Engineering Sciences **454**, 903 (1998).

[26]G. Rilling, P. Flandrin, and P. Gonçalves, in *IEEE-EURASIP Workshop on Nonlinear Signal and Image Processing NSIP-03* (2003).

[27]M. Torres, M. Colominas, G. Schlotthauer, and P. Flandrin, in *IEEE Int. Conf. on Acoust., Speech and Signal Proc. ICASSP-11, Prague (CZ)* (2011) pp. 4144–4147.

[28]X. Garbet, G. Falchetto, M. Ottaviani, R. Sabot, A. Sirinelli, and A. Smolyakov, AIP Conference Proceedings **871**, 342 (2006).

[29]C. Nguyen, X. Garbet, and A. I. Smolyakov, Physics of Plasmas **15**, 112502 (2008).

[30]G. R. McKee, R. J. Fonck, M. Jakubowski, K. H. Burrell, K. Hallatschek, R. A. Moyer, D. L. Rudakov, W. Nevins, G. D. Porter, P. Schoch, and X. Xu, Physics of Plasmas **10**, 1712 (2003).

[31]G. D. Conway, B. Scott, J. Schirmer, M. Reich, A. Kendl, and the ASDEX Upgrade Team, Plasma Physics and Controlled Fusion **47**, 1165 (2005).

[32]A. V. Melnikov, V. A. Vershkov, L. G. Eliseev, S. A. Grashin, A. V. Gudozhnik, L. I. Krupnik, S. E. Lysenko, V. A. Mavrin, S. V. Perfilov, D. A. Shelukhin, S. V. Soldatov, M. V. Ufimtsev, A. O. Urazbaev, G. V. Oost, and L. G. Zimeleva, Plasma Physics and Controlled Fusion **48**, S87 (2006).

[33]A. Krämer-Flecken, S. Soldatov, D. Reiser, M. Kantor, and H. R. Koslowski, Plasma Physics and Controlled Fusion **51**, 015001 (2009).

[34]K. Hallatschek and D. Biskamp, Phys. Rev. Lett. **86**, 1223 (2001).

[35]V. B. Lebedev, P. N. Yushmanov, P. H. Diamond, S. V. Novakovskii, and A. I. Smolyakov, Physics of Plasmas **3**, 3023 (1996).

[36]T. Watari, Y. Hamada, A. Fujisawa, K. Toi, and K. Itoh, Physics of Plasmas **12**, 062304 (2005).

[37]H. Sugama and T.-H. Watanabe, Journal of Plasma Physics **72**, 825 (2006).

[38]D. Zarzoso, X. Garbet, Y. Sarazin, R. Dumont, and V. Grandgirard, Physics of Plasmas **19**, 022102 (2012).

[39]G. D. Conway and the ASDEX Upgrade Team, Plasma Physics and Controlled Fusion **50**, 085005 (2008).

[40]N. Miyato, Y. Kishimoto, and J. Q. Li, Plasma Physics and Controlled Fusion **48**, A335 (2006).

[41]M. N. Rosenbluth and F. L. Hinton, Phys. Rev. Lett. **80**, 724 (1998).

[42]Z. Gao, Physics of Plasmas **17**, 092503 (2010).

[43]W. Guo, S. Wang, and J. Li, Physics of Plasmas **17**, 112510 (2010).

[44]A. D. Gurchenko, E. Z. Gusakov, A. B. Altukhov, E. P. Selyunin, L. A. Esipov, M. Y. Kantor, D. V. Kouprienko, S. I. Lashkul, A. Y. Stepanov, and F. Wagner, Plasma Physics and Controlled Fusion **55**, 085017 (2013).

[45]H. Ren, Physics of Plasmas **21**, 044505 (2014).

[46]R. J. F. Sgalla, A. I. Smolyakov, A. G. Elfimov, and M. F. Bashir, Physics Letters A **377**, 303 (2013).

[47]G. D. Kerbel and M. G. McCoy, Physics of Fluids **28**, 3629 (1985).

[48]Zonca, F. and Chen, L., EPL **83**, 35001 (2008).

[49]B. Davies, Journal of Computational Physics **66**, 36 (1986).

[50]R. Singh, A. Storelli, O. D. Gürcan, P. Hennequin, L. Vermare, P. Morel, and R. Singh, "Geodesic acoustic modes in a fluid model of tokamak plasma : the effects of finite beta and collisionality," (submitted to Physics of Plasmas).

[51]T. Ido, Y. Miura, K. Kamiya, Y. Hamada, K. Hoshino, A. Fujisawa, K. Itoh, S.-I. Itoh, A. Nishizawa, H. Ogawa, Y. Kusama, and J.-M. group, Plasma Physics and Controlled Fusion **48**, S41 (2006).

[52]K. J. Zhao, T. Lan, J. Q. Dong, L. W. Yan, W. Y. Hong, C. X. Yu, A. D. Liu, J. Qian, J. Cheng, D. L. Yu, Q. W. Yang, X. T. Ding, Y. Liu, and C. H. Pan, Phys. Rev. Lett. **96**, 255004 (2006).

[53]L. Yan, J. Cheng, W. Hong, K. Zhao, T. Lan, J. Dong, A. Liu, C. Yu, D. Yu, J. Qian, Y. Huang, Q. Yang, X. Ding, Y. Liu, and C. Pan, Nuclear Fusion **47**, 1673 (2007).

[54]T. Lan, A. D. Liu, C. X. Yu, L. W. Yan, W. Y. Hong, K. J. Zhao, J. Q. Dong, J. Qian, J. Cheng, D. L. Yu, and Q. W. Yang, Physics of Plasmas **15**, 056105 (2008).

[55]J. C. Hillesheim, W. A. Peebles, T. A. Carter, L. Schmitz, and T. L. Rhodes, Physics of Plasmas **19**, 022301 (2012).

[56]C. A. de Meijere, S. Coda, Z. Huang, L. Vermare, T. Vernay, V. Vuille, S. Brunner, J. Dominski, P. Hennequin, A. Krämer-Flecken, G. Merlo, L. Porte, and L. Villard, Plasma Physics and Controlled Fusion **56**, 072001 (2014).

[57]Z. Gao, Physics of Plasmas **20**, 032501 (2013).

[58]C. Wahlberg, Phys. Rev. Lett. **101**, 115003 (2008).

[59]D. Zhou, Physics of Plasmas **17**, 102505 (2010).

[60]C. Fenzi, X. Garbet, E. Trier, P. Hennequin, C. Bourdelle, T. Aniel, G. Colledani, P. Devynck, C. Gil, O. D. Gürcan, L. Manenc, M. Schneider, J.-L. Segui, and the Tore Supra team, Nuclear Fusion **51**, 103038 (2011).

[61]T. Watari, Y. Hamada, A. Nishizawa, and J. Todoroki, Physics of Plasmas **14**, 112512 (2007).

[62]I. Chavdarovski and F. Zonca, Plasma Physics and Controlled Fusion **51**, 115001 (2009).

[63]F. Jenko, W. Dorland, M. Kotschenreuther, and B. N. Rogers, Physics of Plasmas **7**, 1904 (2000).

[64]S. V. Novakovskii, C. S. Liu, R. Z. Sagdeev, and M. N. Rosenbluth, Physics of Plasmas **4**, 4272 (1997).

[65]Z. Gao, K. Itoh, H. Sanuki, and J. Q. Dong, Physics of Plasmas **15**, 072511 (2008).

[66]K. Miki, Y. Kishimoto, N. Miyato, and J. Q. Li, Phys. Rev. Lett. **99**, 145003 (2007).

[67]G. R. McKee, R. J. Fonck, M. Jakubowski, K. H. Burrell, K. Hallatschek, R. A. Moyer, W. Nevins, D. L. Rudakov, and X. Xu, Plasma Physics and Controlled Fusion **45**, A477 (2003).

[68]Y. Hamada, T. Watari, A. Nishizawa, T. Ido, M. Kojima, Y. Kawasumi, K. Toi, and the JIPPT-IIU Group, Plasma Physics and Controlled Fusion **48**, S177 (2006).

[69]J. Cheng, L. Yan, K. Zhao, J. Dong, W. Hong, J. Qian, Q. Yang, X. Ding, X. Duan, and Y. Liu, Nuclear Fusion **49**, 085030 (2009).

[70]P. Hennequin, R. Sabot, C. Honoré, G. T. Hoang, X. Garbet, A. Truc, C. Fenzi, and A. Quéméneur, Plasma Physics and Controlled Fusion **46**, B121 (2004).

[71]Z. Qiu, F. Zonca, and L. Chen, Plasma Physics and Controlled Fusion **52**, 095003 (2010).

[72]C. P. Hung and A. B. Hassam, Physics of Plasmas **20**, 092107 (2013).

[73]R. Hager and K. Hallatschek, Phys. Rev. Lett. **108**, 035004 (2012).

[74]Y. Xu, I. Shesterikov, M. V. Schoor, M. Vergote, R. R. Weynants, A. Krämer-Flecken, S. Zoletnik, S. Soldatov, D. Reiser, K. Hallatschek, C. Hidalgo, and the TEXTOR Team, Plasma Physics and Controlled Fusion **53**, 095015 (2011).

[75]R. Hager and K. Hallatschek, Plasma Physics and Controlled Fusion **55**, 035009 (2013).

[76]X. Garbet, Y. Sarazin, F. Imbeaux, P. Ghendrih, C. Bourdelle, O. D. Gürcan, and P. H. Diamond, Physics of Plasmas **14**, 122305 (2007).